nature nanotechnology

ARTICLES

PUBLISHED ONLINE: 12 OCTOBER 2015 | DOI: 10.1038/NNANO.2015.230

Improved air stability of perovskite solar cells via solution-processed metal oxide transport layers

Jingbi You[1†], Lei Meng[1†], Tze-Bin Song[1], Tzung-Fang Guo[2], Yang (Michael) Yang[1], Wei-Hsuan Chang[1], Ziruo Hong[1], Huajun Chen[1], Huanping Zhou[1], Qi Chen[1], Yongsheng Liu[1], Nicholas De Marco[1] and Yang Yang[1]*

Lead halide perovskite solar cells have recently attracted tremendous attention because of their excellent photovoltaic efficiencies. However, the poor stability of both the perovskite material and the charge transport layers has so far prevented the fabrication of devices that can withstand sustained operation under normal conditions. Here, we report a solution-processed lead halide perovskite solar cell that has p-type NiO_x and n-type ZnO nanoparticles as hole and electron transport layers, respectively, and shows improved stability against water and oxygen degradation when compared with devices with organic charge transport layers. Our cells have a p–i–n structure (glass/indium tin oxide/NiO_x/perovskite/ZnO/Al), in which the ZnO layer isolates the perovskite and Al layers, thus preventing degradation. After 60 days storage in air at room temperature, our all-metal-oxide devices retain about 90% of their original efficiency, unlike control devices made with organic transport layers, which undergo a complete degradation after just 5 days. The initial power conversion efficiency of our devices is 14.6 ± 1.5%, with an uncertified maximum value of 16.1%.

In 2009, Mihasaka and colleagues incorporated perovskite semiconductors into photovoltaic devices and reported a power conversion efficiency (PCE) of ~4%[1]. Since then, significant progress has been made in both the design and optimization of perovskite solar cells. Using mesoporous and planar structures, several groups have reported devices with PCE values of over 15%[2–13]. Organic transport layers, such as poly(3,4-ethylenedioxythiophene) polystyrene sulphonate (PEDOT:PSS)[12,13], 2,2′,7,7′-tetrakis(*N*,*N*-*p*-dimethoxyphenylamino)-9,9′-spirobifluorene (spiro-OMeTAD)[2–5], poly[bis(4-phenyl)(2,4,6-trimethylphenyl)amine] (PTAA)[6,7] and poly(3-hexylthiophene-2,5-diyl) (P3HT)[14], have been used as p-type hole transport layers, and [6,6]-phenyl C_{61} butyric acid methyl ester (PCBM)[12,13], C_{60} and their derivatives[15,16] have been used as n-type electron transport layers. Due to their low energy of formation, organic lead iodide perovskites are also susceptible to degradation in moisture and air[17]. The charge transport layer therefore plays a key role in protecting the perovskite photoactive layer from exposure to such environments, thus achieving highly stable perovskite-based photovoltaic cells. In this fast growing field, selection of the charge transport material has become crucial, not only for energy level matching and charge transport, but also in order to achieve high stability. Although incorporating organic charge transport layers can provide high efficiencies and reduced hysteresis, concerns remain regarding device stability and the cost of fabrication. Recently, several groups have attempted to replace these organic transport layers with inorganic materials such as CuSCN[18], CuI[19] and NiO_x[20,21] as the hole transport layers and ZnO[22] and TiO_2[2–11] as the n-type transport layers. It is known that metal oxides demonstrate much higher carrier mobility and superior stability than the above-mentioned organic materials[23,24]. In addition, metal oxides can be processed easily via solution from corresponding precursors and nanoparticles at low temperatures.

In this Article, we report perovskite solar cells that have all-solution-processed metal oxide charge transport layers. Specifically, we use p-type NiO_x and n-type ZnO nanoparticle films as the hole and electron transport layers, respectively. We demonstrate perovskite solar cells based on all-metal-oxide charge transport layers that show 16.1% efficiency and significantly improved stability compared with cells made with organic layers. We investigate degradation mechanisms and derive important guidelines for future device design with a view to achieving both highly efficient and stable solar devices.

Metal oxide nanoparticle properties

Atomic force microscopy (AFM) was used to characterize the NiO_x and ZnO films. Figure 1 presents AFM images of an ~80-nm-thick NiO_x film (Fig. 1a) and an ~70-nm-thick ZnO film (Fig. 1b) on an indium tin oxide (ITO) substrate. The dense NiO_x film consists of particles with sizes ranging from 50 to 100 nm that effectively serve as a hole-transport layer with electron-blocking properties. This NiO_x film was obtained from nickel nitride precursors (unlike previously reported films, which were fabricated using nickel formate dehydrate[20] or nickel acetate tetrahydrate[25]) in accordance with previous reports describing high-quality metal oxide films grown from nitride salt precursors[26]. An AFM image of the ZnO film obtained via spin-coating of a nanoparticle solution is shown in Fig. 1b. This ZnO nanoparticle film exhibits a continuous and smooth surface with a roughness of <2 nm and a particle size of <10 nm (Supplementary Fig. 1). Scanning Kelvin probe microscopy (SKPM) was then used to examine the electrical properties of the metal oxide films. The work functions of the NiO_x and ZnO were measured to be ~5.2 and 4.45 eV, respectively (Supplementary Fig. 2). The small potential deviation observed indicates that the metal oxide films possess consistent electrical properties across the entire film.

It is also essential for the metal oxide transport layers (especially the NiO_x) to demonstrate low absorption in order to minimize optical losses within the thin-film photovoltaic device.

[1]Department of Material Science and Engineering, University of California, Los Angeles, California 90095, USA. [2]Department of Photonics, Advanced Optoelectronic Technology Center, National Cheng Kung University, Tainan, Taiwan 701, ROC. †These authors contributed equally to this work.
*e-mail: yangy@ucla.edu

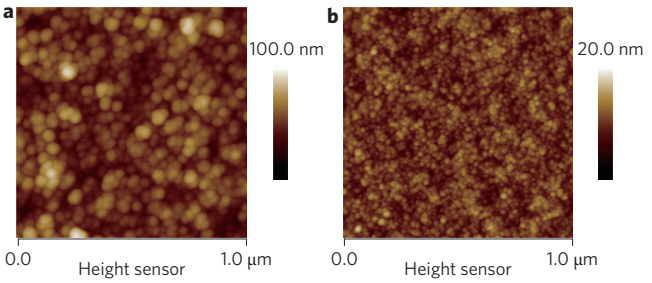

Figure 1 | Morphology of solution-processed metal oxides. a,b, AFM images of NiO_x (**a**) and ZnO (**b**) on an ITO substrate. The particle sizes of NiO and ZnO are ~80 and 10 nm, respectively.

Transmission spectra of the NiO_x (80 nm) and ZnO (70 nm) films are provided in Supplementary Fig. 3. The NiO_x films show relatively high transmittance in the 300–900 nm range, with the exception of a small portion in the lower visible region that may result from defect-related absorption[20,25]. Similarly, the ZnO films show good transmittance.

X-ray photoelectron spectroscopy (XPS) and ultraviolet photoelectron spectroscopy (UPS) measurements were carried out to elucidate the chemical compositions and band alignment of the NiO_x and ZnO films. Figure 2a presents XPS spectra of the Ni $2p_{3/2}$ peaks in NiO_x, which can be separated into three distinct peaks that are consistent with previous reports for NiO_x films obtained via sol–gel or sputtering methods[25,27]. The peak centred at a binding energy of 853.8 eV pertains to Ni^{2+}, characteristic of the standard Ni–O octahedral bonding configuration of the cubic NiO_x rock salt[25]. The peak centred at 855.5 eV was ascribed to a vacancy-induced Ni^{3+} ion, and the broad peak centred at 861.1 eV was attributed to a shake-up process[25]. Figure 2b shows XPS spectra for O 1*s* in NiO_x, with a peak centred at 529.7 eV, further confirming the octahedral bonding of Ni–O. The peak at 531.6 eV may be ascribed to nickel hydroxides, including defective nickel oxides with hydroxyl groups adsorbed onto the surface[25]. The difference between the valence band and Fermi level of NiO_x is ~0.2 eV, based on the valence band spectra provided in Supplementary Fig. 4. This confirms the p-type nature of the NiO_x metal oxide. The workfunction of NiO_x is 5.05 eV, as determined by UPS (Fig. 2c), which is higher than that of the conventional organic hole transport layer PEDOT:PSS (4.9 eV, Fig. 2c). The workfunction of NiO_x is closer to the valence band (VB) of perovskite ($CH_3NH_3PbI_3$) than that of PEDOT:PSS, indicating that a higher V_{OC} may be obtained for the devices, as will be shown in the following sections. The Zn $2p_{3/2}$ (located at 1,021.5 eV) and O 1*s* XPS spectra of ZnO are shown in Fig. 2d,e, respectively. The O 1*s* XPS spectrum for ZnO exhibits a degree of asymmetry in its shape[28], where the peak with lower binding energy (530.1 eV) corresponds to O atoms in the ZnO crystal and the second peak (531.7 eV) is attributed to the presence of an oxygen-deficient component, such as zinc hydroxide[28]. The valence band maximum (VBM, determined via linear extrapolation of the leading edges of the valence band spectra) spectrum (Supplementary Fig. 4) confirms the n-type nature of the ZnO used in this work. The work function of ZnO is 4.2 eV, as determined by UPS (Fig. 2f). For comparison, the UPS spectrum of the PCBM film is also included in Fig. 2f. It is found that the work functions of PCBM and ZnO are similar and close to the conduction band (CB) of $CH_3NH_3PbI_3$ (ref. 2).

Charge transfer, film crystallinity and device structure

On contact with charge transport layers, perovskite films typically exhibit strong photoluminescence quenching as evidence of efficient charge transfer from the photoactive layer to the transport layer. Figure 3a shows the steady-state photoluminescence of glass/perovskite, glass/NiO_x/perovskite and glass/perovskite/ZnO. A clear quenching of photoluminescence emission by both the NiO_x and ZnO layers is observed. Time-resolved photoluminescence (TRPL) measurements of the $CH_3NH_3PbI_3$ show a decrease in the photoluminescence lifetime of the perovskite layer from 145 ns to 70 and 21 ns in the presence of NiO_x and ZnO, respectively, indicating that charge carriers within the perovskite layer can be extracted effectively by these metal oxides[29,30]. For

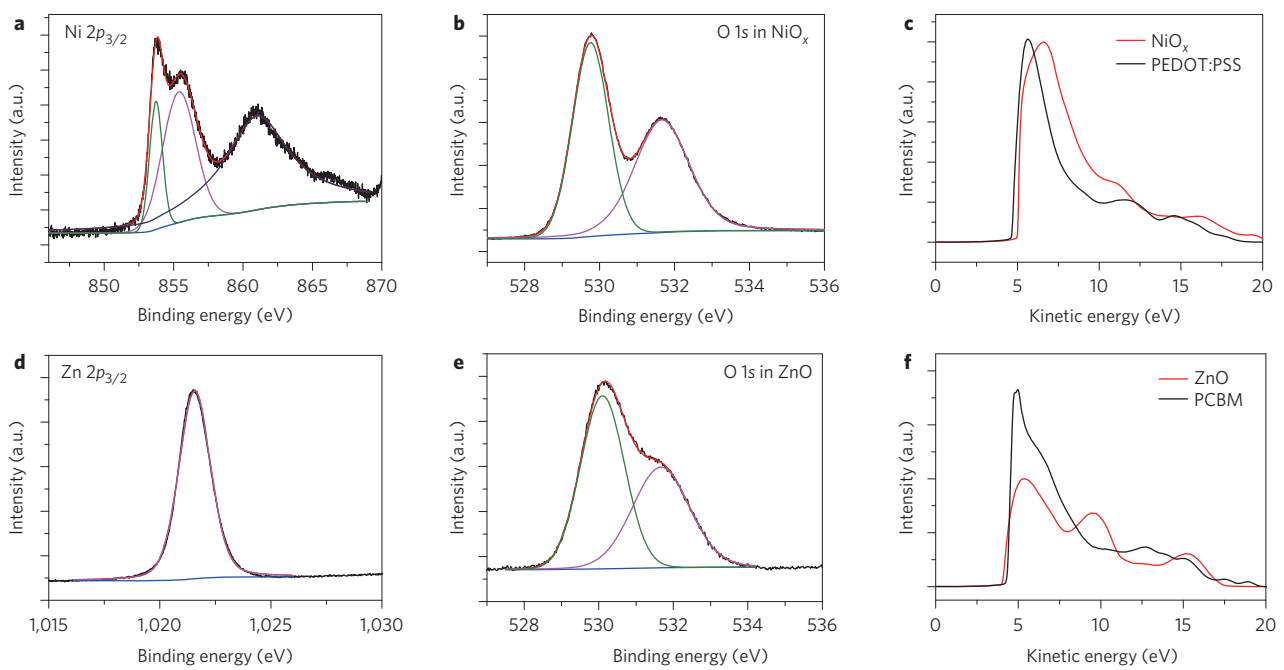

Figure 2 | Electronic states of the NiO_x and ZnO nanoparticle films. a,b, XPS spectra depicting the Ni $2p_{3/2}$ peaks (**a**) and O 1s peaks (**b**) of the NiO_x films. **c**, UPS measurements of NiO_x and PEDOT:PSS films. **d,e**, XPS spectra of Zn $2p_{3/2}$ peaks (**d**) and O 1s peaks (**e**) characteristic of ZnO. **f**, UPS measurements for ZnO and PCBM. For **a,b,d,e**: measured results, black line; fitting curve, red line; background, blue line; sub-peaks fitting, other colours.

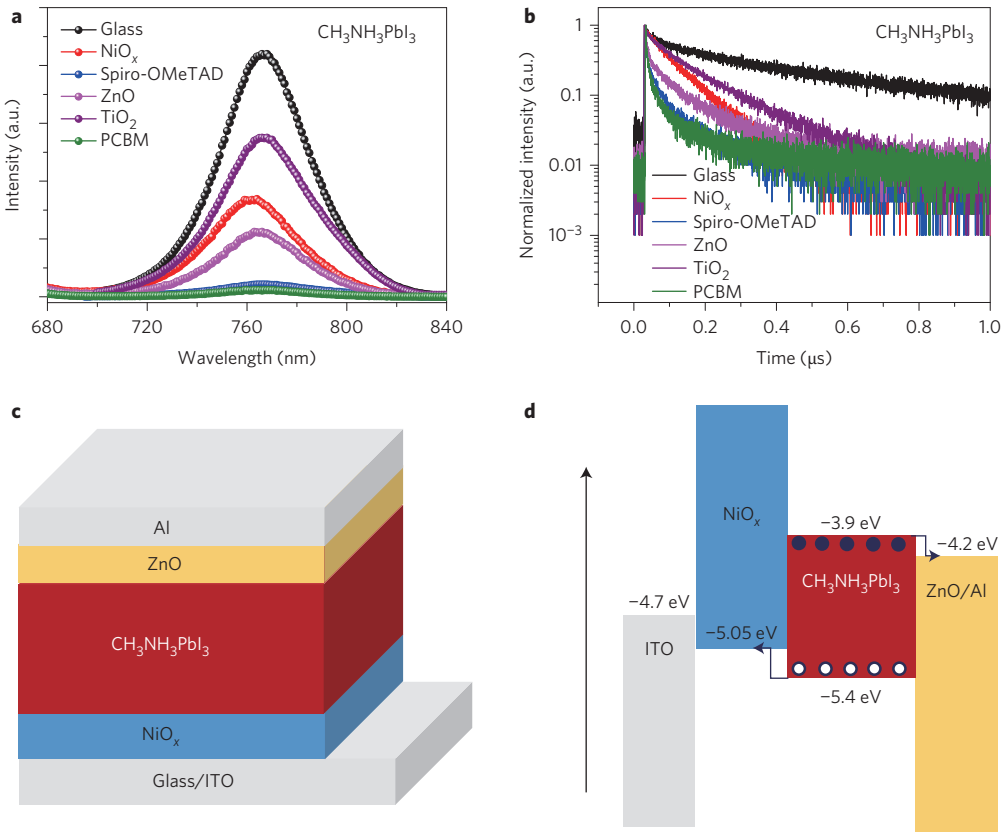

Figure 3 | Charge transport properties of the metal oxide and perovskite, with corresponding device structure. a, Photoluminescence of $CH_3NH_3PbI_3$ contacted with different interfaces: glass, NiO_x, spiro-OMeTAD, ZnO, TiO_2 and PCBM. **b**, TRPL data for $CH_3NH_3PbI_3$ contacted with different interfaces: glass, NiO_x, spiro-OMeTAD, ZnO, TiO_2 and PCBM. **c**, Overall device structure, consisting of glass/ITO/NiO_x/$CH_3NH_3PbI_3$/ZnO/Al. **d**, Energy band alignment of the metal-oxide-based perovskite solar cell according to UPS measurements from Fig. 2c,f.

comparison, the quenching behaviour between perovskite ($CH_3NH_3PbI_3$) and other common transport layers (spiro-OMeTAD, TiO_2 and PCBM) was also investigated. The steady-state and TRPL measurements for these structures are shown in Fig. 3a,b. It was found that the spiro-OMeTAD and PCBM show a stronger quenching effect than the NiO_x and ZnO, respectively, while TiO_2 exhibits less quenching than ZnO[29]. The relationship between device performance and interfacial quenching will be the subject of future investigation.

The device structure of the all-metal-oxide-based perovskite solar cell is shown in Fig. 3c. This consists of glass/ITO/NiO_x/perovskite ($CH_3NH_3PbI_3$)/ZnO/Al, where the NiO_x and ZnO act as the hole and electron transport layers, respectively. The band diagram for this structure is shown in Fig. 3d using the workfunctions of NiO_x and ZnO measured in this work (Fig. 2)[2]. On exposure to light, charge carriers are generated in the perovskite layer, and electrons and holes are subsequently collected by their respective contacts, ZnO and NiO_x.

X-ray diffraction (XRD) patterns for perovskite films deposited on NiO_x-coated ITO substrates are shown in Supplementary Fig. 5, in which all the diffraction peaks originate from $CH_3NH_3PbI_3$ except for the one at 12.6°, which indicates a small amount of residual PbI_2 (ref. 4). The crystal structure of the perovskite formed on the NiO_x surface is β-phase[31]. The crystallinity of perovskite films constructed via a two-step method differs from those formed in one step, which usually have a (110) preferred orientation[12,30]. Scanning electron microscopy (SEM) images of the perovskite film on NiO_x are shown in Fig. 4a. The film consists of large crystals with dimensions greater than 1 μm and shows no observable pinholes. The perovskite films grown on PEDOT:PSS have grain sizes of ~300–500 nm (Supplementary Fig. 6). This difference in crystal size strongly suggests that the NiO_x surface provides better crystallinity of the perovskite film, possibly due to surface effects that may provide effective nucleation sites to initiate perovskite crystal growth. A top-view SEM image of the perovskite film capped by a ZnO layer is shown in Fig. 4b, which shows full coverage of the perovskite film by ZnO nanoparticles. A cross-sectional image of the device (Al electrode not included) is shown in Fig. 4c. The individual layers of NiO_x/perovskite/ZnO can be distinguished easily, and have thicknesses of 80, 320 and 70 nm, respectively. Note that charge transport and collection occur along the vertical direction in a single crystal grain without grain boundary interference.

Device performances

The dependence of device performance on NiO_x thickness was investigated based on a device with the structure glass/ITO/NiO_x/$CH_3NH_3PbI_3$/PCBM/Al. The results for different thicknesses of NiO_x are presented in Supplementary Fig. 7a and are summarized in Supplementary Table 1. It was found that when the NiO_x layer is too thin (for example, 20 nm), the devices show current leakage and low shunt resistance, resulting in a low open-circuit voltage and fill factor (FF), which could be due to the poor coverage of NiO_x on the ITO surface. On the other hand, the series resistance will increase if the NiO_x layer is too thick (for example, 120 nm), which will also reduce the FF. Devices with a NiO_x thickness of 40 nm show better performance, still with a little leakage, while devices of 80 nm have the highest FF and best performance. Device performance distributions with different thicknesses of NiO_x are shown in Supplementary Fig. 8. Although the performances show some variation, it is clear that a NiO_x thickness of 80 nm

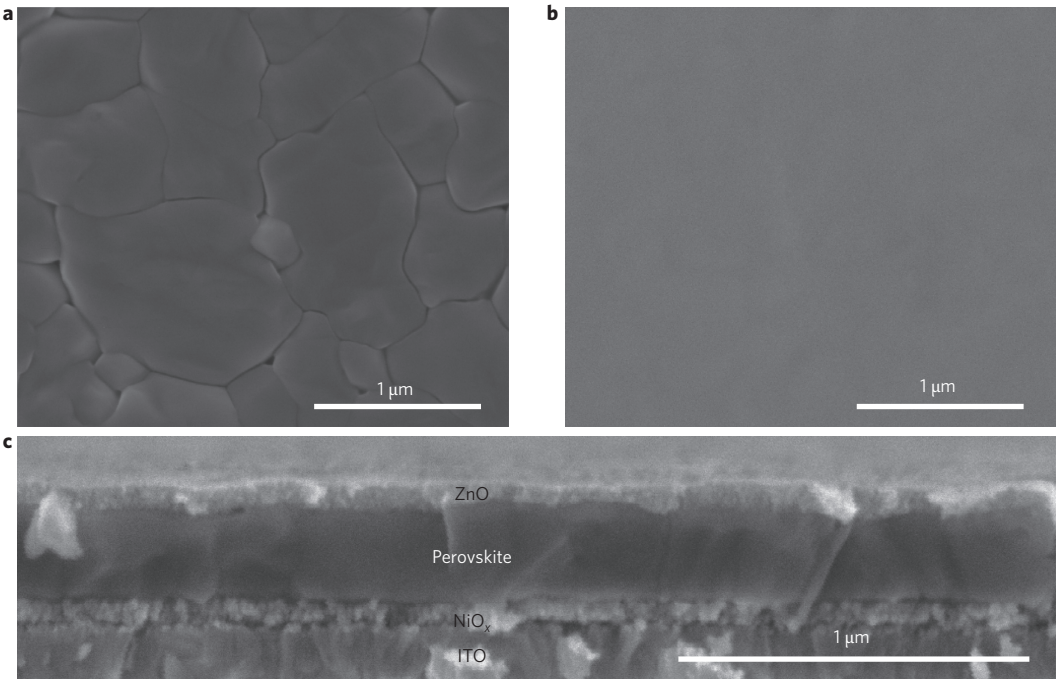

Figure 4 | Morphology of perovskite film and device. a, SEM image of perovskite growth on a NiO_x surface achieved by two-step solution processing. **b**, SEM image of perovskite coated with ZnO films. **c**, Cross-sectional image of a device (the unfinished Al electrode is not included) with the structure glass/ITO/NiO_x/perovskite/ZnO, with NiO_x, perovskite ($CH_3NH_3PbI_3$) and ZnO thicknesses of 80, 320 and 70 nm, respectively.

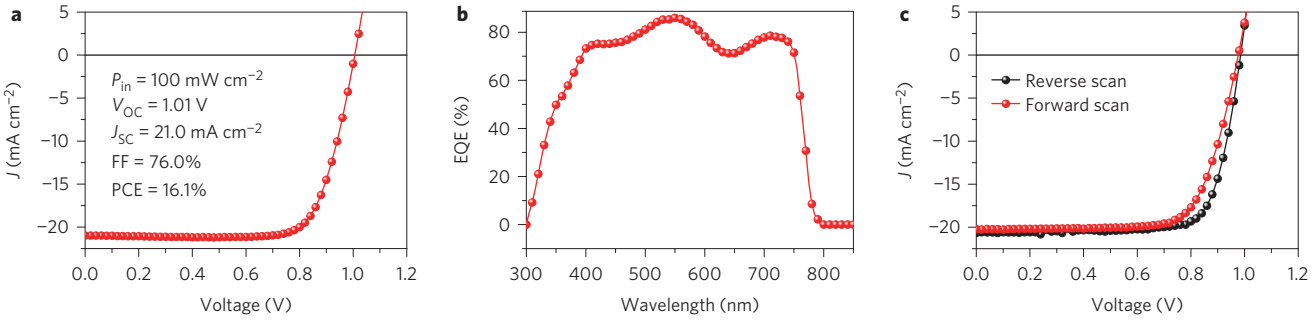

Figure 5 | Device performance of metal-oxide-based perovskite solar cells (glass/ITO/NiO_x/$CH_3NH_3PbI_3$/ZnO/Al). a, *J–V* curve of the best device under one sun conditions (100 mW cm^{-2}, AM 1.5G). **b**, EQE of the metal-oxide-based perovskite solar cell. **c**, Typical *J–V* curve obtained by reverse scan (1.2 V → 0 V, step 0.02 V, delay time 200 ms) and forward scan (0 V → 1.2 V, step 0.02 V, delay time 200 ms) for the metal-oxide-based devices.

gives the best device performance, and thinner or thicker NiO_x films yield inferior device performance. It was also found that the optimum thickness of ZnO as the electron transport layer is ~70 nm (Supplementary Fig. 7b and Supplementary Table 2). The device performance distribution is summarized in Supplementary Fig. 9, which indicates good reproducibility. The PCE of our devices was 14.6 ± 1.5% (uncertified). The best device performances for the all-metal-oxide-based devices are presented in Fig. 5a, achieving a V_{OC} of 1.01 V, J_{SC} of 21.0 mA cm^{-2} and FF of 76.0%, leading to an overall device efficiency of 16.1%. Based on an identical perovskite film, the NiO_x hole transport layer produces a higher V_{OC} than with PEDOT:PSS, and the ZnO-based device a higher J_{SC} compared with those using PCBM as an electron transport layer (Supplementary Figs 10–12 and Supplementary Tables 3–5). The higher V_{OC} from the NiO_x-based device could stem from two factors. The first is a more favourable band alignment between the hole transport layer and the perovskite film, where the VBs of NiO_x and PEDOT:PSS were determined to be 5.05 and 4.9 eV (Fig. 2). The deep VB of the NiO_x could form a better ohmic contact with the perovskite layer, leading to a larger potential difference between the hole and electron transport layers[20,32]. The second factor is an improved crystallinity of the perovskite film on NiO_x compared with that formed on PEDOT:PSS (Fig. 4 and Supplementary Fig. 6). The larger crystal size will reduce the number of grain boundaries, which could decrease recombination[12]. Both factors could lead to a higher open-circuit voltage using NiO_x as the hole transport layer rather than PEDOT:PSS[12,32]. The higher J_{SC} resulting from the ZnO-based devices may be attributed to a strong hole-blocking effect originating from the deep VB of ZnO and/or the optical spacer effect[33,34]. The external quantum efficiency (EQE) of the all-metal-oxide-based device is shown in Fig. 5b, and EQE integration over an AM 1.5G spectrum delivers a J_{SC} value consistent with the corresponding *J–V* measurement.

Typical *J–V* curves for the metal-oxide-based device (NiO_x/ZnO interface combination) with different scan directions (reverse and forward) are shown in Fig. 5c, in which a small hysteresis can be observed. There is no, or negligible, *J–V* hysteresis when using PCBM (PEDOT:PSS/PCBM and NiO_x/PCBM interface combinations) as the top electron transport layers (Supplementary Fig. 13 and Supplementary Table 6), which is consistent with

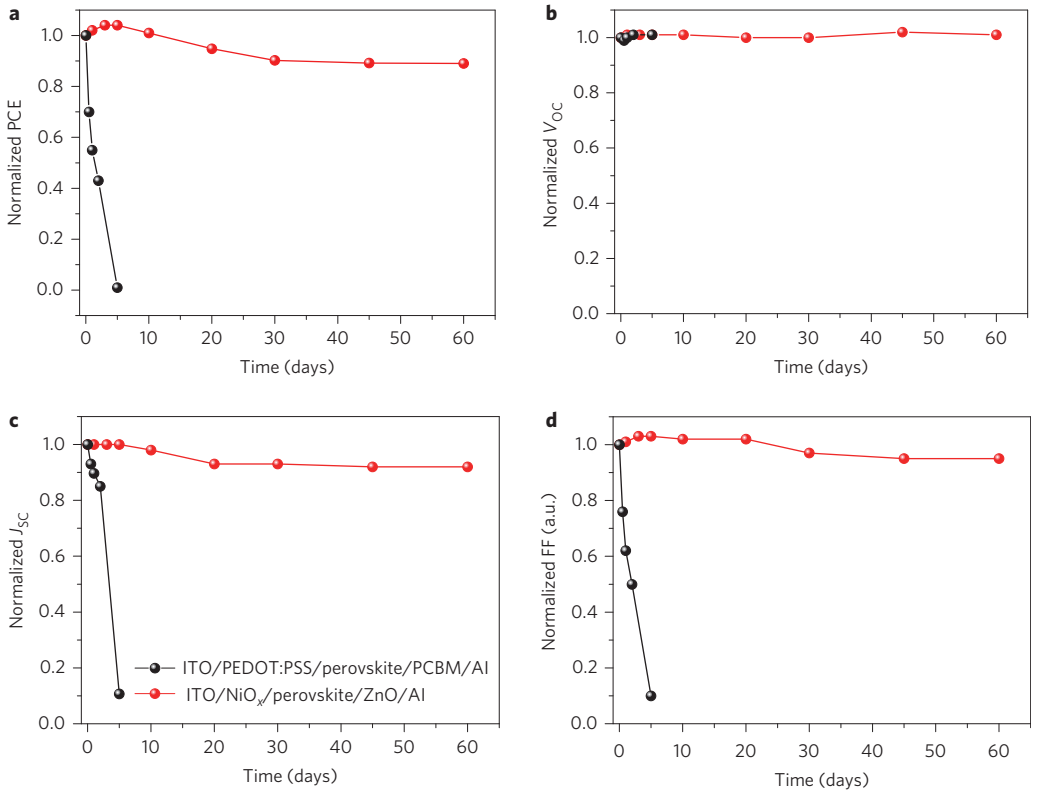

Figure 6 | Stability of the devices in an ambient environment without encapsulation. Device performances of ITO/PEDOT:PSS/perovskite/PCBM/Al (black) and ITO/NiO$_x$/perovskite/ZnO/Al (red) structures as a function of storage time in an ambient environment (30–50% humidity, T = 25 °C). **a**, Normalized PCE. **b**, Normalized V_{OC}. **c**, Normalized J_{SC}. **d**, Normalized FF.

previous results[12,35]. Hysteresis is still a largely controversial issue in perovskite solar cells[6,36], but more and more results have recently supported the proposal that the hysteresis originates from ion motion within the perovskite layer[35,37–40]. When an external field is applied, the ions move to the interface between the perovskite and the charge transport layer, and a temporary dipole forms, which is believed to be the reason for the hysteresis[37–40]. For an inverted structure, n-type PCBM is deposited on the perovskite, which could penetrate/diffuse into the perovskite layer through the pin-holes/grain boundary during processing (spin-coating or annealing[35,37]). Mobile ions in the perovskite could fully interact with PCBM to form a PCBM halide radical[40], which is thought to stabilize electrostatic properties, reducing the electric field-induced anion migration that may give rise to hysteresis and thus resulting in no hysteresis[35,37–40]. It was found that the devices still show obvious hysteresis when the PCBM is used as the bottom electron transport layer[41], which could be explained by the fact that the perovskite and PCBM cannot penetrate into one another, and the ion movement in perovskite cannot be fully suppressed[40]. In the case of the metal oxide transport layers, the large metal oxide particles cannot easily diffuse into the perovskite layer and, more importantly, there is no ionic interaction between the perovskite and the metal oxide, so the ions will remain free to move around with changing bias[38], resulting in the observed hysteresis (Fig. 5c).

Device stability

In spite of the high photovoltaic efficiency, one major concern is whether perovskite solar cells are durable for terrestrial applications[42]. We therefore monitored the stability of these devices using both inorganic and organic charge transport layers. Devices were tested without encapsulation (the devices were exposed directly to the environment, without any cover) in an ambient environment at 25 °C and with 30–50% humidity. As shown in Fig. 6a, in terms of the PCE of the metal-oxide-based devices, the majority of the original device performance was retained for up to 60 days (for J–V curves see Supplementary Fig. 10). However, devices based on the organic charge transport layers degraded dramatically, with a drop in efficiency to close to zero after only 5 days (Fig. 6a and Supplementary Fig. 11). The degradation of key photovoltaic parameters, that is, J_{SC}, V_{OC} and FF versus time, is summarized in Fig. 6b–d.

Possible degradation mechanisms occurring when using PCBM may be due to (1) the adsorption of oxygen/water by the PCBM[43] and (2) incomplete coverage of the perovskite film by the PCBM, thus providing insufficient protection and leading to a rapid chemical reaction between the Al electrode and the perovskite and/or further exposure to the ambient environment.

It was found that the PCBM layer can itself degrade in ambient air through adsorption of oxygen or water[43]. The XPS results identified an additional peak due to the water–PCBM interaction, and the UPS data showed an increase in the lowest occupied molecular orbital (LUMO) of PCBM (Supplementary Fig. 14). As a result, the degraded PCBM film showed a large contact resistance with the adjacent Al layer (Supplementary Fig. 15), which is consistent with the dark J–V curve for the degraded devices (Supplementary Fig. 11).

In addition to degradation of the PCBM layer itself, the chemical reaction between the perovskite and the electrode is another major concern for device stability. Metals such as Al and Ag are commonly used as electrodes and can react with the perovskite film under humid conditions or when in direct contact with one another, according to our experimental evidence (Supplementary Fig. 16). Transmission electron microscopy (TEM) results (Supplementary Fig. 17) indicated that metals such as Al can diffuse into the PCBM layer to a depth as great as 10 nm during evaporation of the metal[44,45]. This increases the possibility of direct physical contact between the perovskite and Al layer in the thinner electron transport layer locations, which would undoubtedly result in

decomposition of the perovskite photoactive layer and severe damage to the metal electrode (Supplementary Fig. 18). A thicker PCBM layer could potentially isolate the perovskite from the electrode and partially avoid such a chemical reaction (Supplementary Fig. 16). However, this would also result in devices with poor performances due to the limited mobility of the PCBM (Supplementary Fig. 19)[46].

Through replacement of PCBM with ZnO in an ITO/PEDOT:PSS/perovskite/ZnO/Al device structure, a significant enhancement in stability was achieved (Supplementary Fig. 12). The metal oxide ZnO showed good stability in ambient air (Supplementary Fig. 15), and the dense ZnO was able to completely isolate the perovskite and Al electrode layers from one another (Supplementary Fig. 16). Finally, the ZnO may serve as a robust diffusion barrier (similar to TiO_2) against water due to its scavenging effects[47].

Furthermore, we have shown that using metal oxide NiO_x as the hole transport layer can further improve the stability when compared with devices using PEDOT:PSS (Supplementary Figs 10 and 12). PEDOT:PSS is commonly used as a hole transport layer, but is generally considered an unstable transport layer for organic devices due to its hydrophilic and acidic nature[48]. The stable p-type metal oxide NiO_x was used to overcome this issue and improve device stability.

Conclusions

In summary, we have successfully demonstrated efficient perovskite solar cells employing all-solution-processed metal oxide charge transport layers. More importantly, it was found that our all-metal-oxide devices show a significant improvement in stability in ambient air compared with devices made with organic transport layers. The mechanism of the improved stability has been discussed. Our results show that metal oxide nanoparticles as transport layers are a promising material with which to construct efficient and stable perovskite solar cells for practical applications.

Methods

Methods and any associated references are available in the online version of the paper.

Received 6 January 2015; accepted 3 September 2015; published online 12 October 2015

References

1. Kojima, A., Teshima, K., Shirai, Y. & Miyasaka, T. Organometal halide perovskites as visible-light sensitizers for photovoltaic cells. *J. Am. Chem. Soc.* **131,** 6050–6051 (2009).
2. Kim, H. S. *et al.* Lead iodide perovskite sensitized all-solid-state submicron thin film mesoscopic solar cell with efficiency exceeding 9%. *Sci. Rep.* **2,** 591 (2012).
3. Lee, M. M. *et al.* Efficient hybrid solar cells based on meso-superstructured organometal halide perovskites. *Science* **338,** 643–647 (2012).
4. Burschka, J. *et al.* Sequential deposition as a route to high-performance perovskite-sensitized solar cells. *Nature* **499,** 316–319 (2013).
5. Liu, M., Johnston, M. B. & Snaith, H. J. Efficient planar heterojunction perovskite solar cells by vapour deposition. *Nature* **501,** 395–398 (2013).
6. Jeon, N. J. *et al.* Solvent engineering for high-performance inorganic–organic hybrid perovskite solar cells. *Nature Mater.* **13,** 897–903 (2014).
7. Yang, W. S. *et al.* High-performance photovoltaic perovskite layers fabricated through intramolecular exchange. *Science* **348,** 1234–1237 (2015).
8. Im, J. H., Jang, I. H., Pellet, N., Grätzel, M. & Park, N. G. Growth of $CH_3NH_3PbI_3$ cuboids with controlled size for high-efficiency perovskite solar cells. *Nature Nanotech.* **9,** 927–932 (2014).
9. Zhou, H. *et al.* Interface engineering of highly efficient perovskite solar cells. *Science* **345,** 542–546 (2014).
10. Wojciechowski, K. *et al.* Heterojunction modification for highly efficient organic–inorganic perovskite solar cells. *ACS Nano* **8,** 12701–12709 (2014).
11. Xiao, M. *et al.* A fast deposition–crystallization procedure for highly efficient lead iodide perovskite thin-film solar cells. *Angew. Chem. Int. Ed.* **53,** 9898–9903 (2014).
12. You, J. *et al.* Moisture assisted perovskite film growth for high performance solar cells. *Appl. Phys. Lett.* **105,** 183902 (2014).
13. Xiao, Z. G. *et al.* Efficient, high yield perovskite photovoltaic devices grown by interdiffusion of solution-processed precursor stacking layers. *Energy Environ. Sci.* **7,** 2619–2623 (2014).
14. Conings, B. *et al.* Perovskite-based hybrid solar cells exceeding 10% efficiency with high reproducibility using a thin film sandwich approach. *Adv. Mater.* **26,** 2041–2046 (2014).
15. Jeng, J. Y. *et al.* $CH_3NH_3PbI_3$ perovskite/fullerene planar-heterojunction hybrid solar cells. *Adv. Mater.* **25,** 3727–3732 (2013).
16. Liang, P. W. *et al.* Additive enhanced crystallization of solution-processed perovskite for highly efficient planar-heterojunction solar cells. *Adv. Mater.* **26,** 3748–3754 (2014).
17. Noh, J. H. *et al.* Chemical management for colorful, efficient, and stable inorganic–organic hybrid nanostructured solar cells. *Nano Lett.* **13,** 1764–1769 (2013).
18. Qin, P. *et al.* Inorganic hole conductor-based lead halide perovskite solar cells with 12.4% conversion efficiency. *Nature Commun.* **5,** 3834 (2014).
19. Christians, J. A. *et al.* An inorganic hole conductor for organo-lead halide perovskite solar cells improved hole conductivity with copper iodide. *J. Am. Chem. Soc.* **136,** 758–764 (2014).
20. Jeng, J. Y. *et al.* Nickel oxide electrode interlayer in $CH_3NH_3PbI_3$ perovskite/PCBM planar-heterojunction hybrid solar cells. *Adv. Mater.* **26,** 4107–4113 (2014).
21. Zhu, Z. L. *et al.* High-performance hole-extraction layer of sol–gel-processed NiO_x nanocrystals for inverted planar perovskite solar cells. *Angew. Chem. Int. Ed.* **53,** 12571–12575 (2014).
22. Liu, D. Y. & Kelly, T. L. Perovskite solar cells with a planar heterojunction structure prepared using room-temperature solution processing techniques. *Nature Photon.* **8,** 133–138 (2014).
23. Hau, S. K. *et al.* Air-stable inverted flexible polymer solar cells using zinc oxide nanoparticles as an electron selective layer. *Appl. Phys. Lett.* **92,** 253301 (2008).
24. Qian, L. *et al.* Stable and efficient quantum-dot light-emitting diodes based on solution-processed multilayer structures. *Nature Photon.* **5,** 543–548 (2011).
25. Manders, J. R. *et al.* Solution-processed nickel oxide hole transport layers in high efficiency polymer photovoltaic cells. *Adv. Funct. Mater.* **23,** 2993–3001 (2013).
26. Rim, Y. S. *et al.* Direct light pattern integration of low-temperature solution-processed all-oxide flexible electronics. *ACS Nano* **8,** 9680–9686 (2014).
27. Wang, K. C. *et al.* Low-temperature sputtered nickel oxide compact thin film as effective electron blocking layer for mesoscopic $NiO_x/CH_3NH_3PbI_3$ perovskite heterojunction solar cells. *ACS Appl. Mater. Interfaces* **6,** 11851–11858 (2014).
28. Sun, Y. M. *et al.* Inverted polymer solar cells integrated with a low-temperature-annealed sol-gel-derived ZnO film as an electron transport layer. *Adv. Mater.* **23,** 1679–1683 (2011).
29. Docampo, P. *et al.* Efficient organometal trihalide perovskite planar-heterojunction solar cells on flexible polymer substrates. *Nature Commun.* **4,** 2761 (2013).
30. You, J. *et al.* Low-temperature solution-processed perovskite solar cells with high efficiency and flexibility. *ACS Nano* **8,** 1674–1680 (2014).
31. Stoumpos, C. C. *et al.* Semiconducting tin and lead iodide perovskites with organic cations: phase transitions, high mobilities, and near-infrared photoluminescent properties. *Inorg. Chem.* **52,** 9019–9038 (2013).
32. Park, J. H. *et al.* Efficient $CH_3NH_3PbI_3$ perovskite solar cells employing nanostructured p-type NiO electrode formed by a pulsed laser deposition. *Adv. Mater.* **27,** 4013–4019 (2015).
33. You, J. *et al.* Electroluminescence behavior of ZnO/Si heterojunctions: energy band alignment and interfacial microstructure. *J. Appl. Phys.* **107,** 083701 (2010).
34. Gilot, J. *et al.* The use of ZnO as optical spacer in polymer solar cells: theoretical and experimental study. *Appl. Phys. Lett.* **91,** 113520 (2007).
35. Shao, Y. C., Xiao, Z. G., Bi, C., Yuan, Y. B. & Huang, J. S. Origin and elimination of photocurrent hysteresis by fullerene passivation in $CH_3NH_3PbI_3$ planar heterojunction solar cells. *Nature Commun.* **5,** 5784 (2014).
36. Snaith, H. J. *et al.* Anomalous hysteresis in perovskite solar cells. *J. Phys. Chem. Lett.* **5,** 1511–1515 (2014).
37. Stranks, S. D. & Sanith, H. J. Metal-halide perovskites for photovoltaic and light-emitting devices. *Nature Nanotech.* **10,** 391–402 (2015).
38. Bastiani, M. D., Binda, M., Gandini, M., Ball, J. & Petrozza, A. Charge extraction layer investigation for high efficiency and hysteresis-less organo lead halide perovskite solar cell. *Proc. MRS Spring Meeting* C4.04 (2015).
39. Zhang, Y. *et al.* Charge selective contacts, mobile ions and anomalous hysteresis in organic–inorganic perovskite solar cell. *Mater. Horiz.* **2,** 315–322 (2015).
40. Xu, J. X. *et al.* Perovskite–fullerene hybrid materials suppress hysteresis in planar diodes. *Nature Commun.* **6,** 7081 (2015).
41. Ryu, S. *et al.* Fabrication of metal-oxide-free $CH_3NH_3PbI_3$ perovskite solar cells processed at low temperature. *J. Mater. Chem. A* **3,** 3271–3275 (2015).
42. Mei, A. *et al.* A hole-conductor-free, fully printable mesoscopic perovskite solar cell with high stability. *Science* **345,** 295–298 (2014).
43. Bao, Q. *et al.* Oxygen- and water-based degradation in [6,6]-phenyl-C_{61}-butyric acid methyl ester (PCBM) films. *Adv. Energy Mater.* **4,** 1301272 (2014).
44. Peumans, P. *et al.* Small molecular weight organic thin-film photodetectors and solar cells. *J. Appl. Phys.* **93,** 3693–3722 (2003).

45. Durr, A. C. *et al.* Morphology and thermal stability of metal contacts on crystalline organic films. *Adv. Mater.* **14,** 961–963 (2002).
46. Seo, J. *et al.* Benefits of very thin PCBM and LiF layers for solution-processed p–i–n perovskite solar cells. *Energy Environ. Sci.* **7,** 2642–2646 (2014).
47. Lee, K. H. *et al.* Air-stable polymer electronic devices. *Adv. Mater.* **19,** 2445–2449 (2007).
48. De Jong, M. P. *et al.* Stability of the interface between indium-tin-oxide and poly (3,4-ethylenedioxythiophene)/poly(styrenesulfonate) in polymer light-emitting diodes. *Appl. Phys. Lett.* **77,** 2255–2257 (2000).

Acknowledgements

This work was supported financially by a grant from the National Science Foundation (ECCS-1202231) and the Air Force Office of Scientific Research (FA9550-12-1-0074). T.F.G. acknowledges financial support from the Ministry of Science and Technology (MOST), Taiwan ROC (MOST 103-2119-M-006-020 and MOST 102-2628-M-006-001-MY3). The authors thank E. Zhu and Y. Li for TEM measurement, S. Adam for help with SKPM measurements and Y.S. Rim for discussions regarding NiO_x synthesis. The authors also thank G. Li for discussions and E. Young for proof reading.

Author contributions

J.Y. and Y.Y. designed the experiments. J.Y. and L.M. performed device fabrication and data analysis. T.Z.S., H.C., Y.(M.)Y., W.H.C., H.Z., Q.C., Y.S.L. and N.D.M. contributed materials/analysis tools. T.F.G. commented on the project. J.Y., L.M. and Y.Y. co-wrote the paper. All authors discussed the results and commented on the manuscript.

Additional information

Supplementary information is available in the online version of the paper. Reprints and permissions information is available online at www.nature.com/reprints. Correspondence and requests for materials should be addressed to Y.Y.

Competing financial interests

The authors declare no competing financial interests.

Methods

NiO_x precursor solution. Nickel(II) nitrate hexahydrate ($Ni(NO_3)_2{\cdot}6H_2O$) (Sigma Aldrich) was dissolved in ethylene glycol solution containing 1 M nickel(II) nitrate hexahydrate with ethylenediamine (Aldrich). The solution was spin-cast onto glass/ITO substrate at a spin speed ranging from 1,000 to 4,000 r.p.m. for 90 s to control the NiO_x thickness. The substrate was then post-annealed at 300 °C in ambient air for 60 min.

ZnO nanoparticles synthesis. The chemical synthesis of ZnO nanoparticles was performed using the method outlined in our previous publication[49], but methanol was totally removed to prevent the residual solvent decomposing the perovskite layer, as it has been confirmed that some solvents, such as ethanol and methanol, can degrade/decompose perovskite. After drying the ZnO nanoparticles, the powder was then redispersed in chlorobenzene to a concentration of 2%. The thicknesses of the ZnO layer were controlled by the spin speed.

Device fabrication and measurement. PEDOT:PSS was spin-cast onto the ITO surface at 4,000 r.p.m. and then annealed at 120 °C for 15 min in ambient air. The NiO_x precursor was spin-coated on the ITO and annealed at 300 °C for 60 min in ambient air. The substrates were then transferred into a nitrogen glove box for coating of the perovskite layer, where a two-step spin-coating process was adopted. (It was found that a one-step solution process cannot form a high quality of perovskite film on the NiO_x[20,21], possibly due to the surface roughness of the NiO_x inducing fast crystallization in the perovskite, so the two-step process was adopted here to obtain a sufficiently high quality perovskite layer[35].) The PbI_2 layer was spin-coated first using a 460 mg ml^{-1} solution and dried at 70 °C for 10 min, then 50 mg ml^{-1} of CH_3NH_3I solution was coated onto the PbI_2 layer, after which the film was taken out for annealing in ambient air at 100 °C for 2 h. For PCBM coating, a 2% PCBM in chlorobenzene solution was coated onto the perovskite layer. For the ZnO layer, different thicknesses of ZnO were coated onto the perovskite surface by controlling the spin speed. Finally, the device was transferred to a vacuum chamber for Al electrode evaporation. The device area was 0.1 cm^2. *J–V* characteristics of the photovoltaic cells were measured using a Keithley 2400 source unit under a simulated AM 1.5G spectrum. With an Oriel 9600 solar simulator, the light intensity was calibrated by a KG-5 Si diode. *I–V* measurements were carried out in a nitrogen glove box. The devices were measured in reverse scan (1.2 V → 0 V, step 0.02 V, delay time 200 ms) and forward scan (0 V → 1.2 V, step 0.02 V, delay time 200 ms). The differences between reverse and forward scans are shown in Fig. 5c, Supplementary Fig. 13 and Supplementary Table 6). The devices were taken out for EQE measurements using an Enli tech (Taiwan) EQE measurement system.

SKPM. SKPM was performed on perovskite samples under ambient conditions using a Dimension Icon scanning probe microscope (Bruker Nano) in single-pass frequency-modulated (FM) mode. FM detection maximizes the spatial resolution by measuring the local electrostatic force gradient present solely at the apex of the AFM tip, thereby reducing the contributions of the tip cone and cantilever that are present in the more common amplitude-modulated detection schemes. Application of an off-resonant a.c. voltage (~5 V, 2 kHz) between a conductive AFM probe (heavily doped Si tips, Bruker) and the grounded sample alters the effective spring constant of the cantilever and thus modulates its resonant frequency due to an induced electric force gradient. Spatial variations in the surface potential/workfunction were directly measured by nulling the local electrostatic force gradient arising from contact potential differences between the AFM tip and the film surface by using a bias-controlled feedback loop. A minimum force set-point was applied, as indicated by nominal phase contrast, to reduce potential artefacts in the surface potential images. The workfunction of the Si tip (heavily doped Si tips) was calibrated using a freshly cleaved highly ordered pyrolytic graphite (HOPG) substrate of known workfunction (4.6 eV), and the workfunction of the Si tip used was found to be 4.4 eV.

TEM. High-resolution TEM images and energy-dispersive X-ray spectroscopy (EDS) data were obtained on an FEI TITAN transmission electron microscope operated at 300 kV. The sample glass/ITO/PCBM (30 nm)/Al (30 nm) was used for the TEM sample. The focused ion beam technique was used for cross-TEM sample preparation.

XRD. XRD patterns (θ–2θ scans) were obtained from samples of perovskite deposited on substrates using a double-axis X-ray diffractometer (Bede D1) equipped with a focusing graded X-ray mirror with monochromatic CuKα (λ = 1.5405 Å) radiation source. Scans were taken with a 0.5-mm-wide source and detector slits, and with X-ray generator settings of 40 kV and 30 mA.

SEM. A field-emission scanning electron microscope (FEI Nova 230 NanoSEM) was used to acquire SEM images. The instrument used an electron beam accelerated at 500 V to 30 kV, enabling operation at a variety of currents.

Steady photoluminescence and TRPL. Steady-state photoluminescence was measured using a Horiba Jobinyvon system with excitation at 600 nm. In the TRPL measurement, the samples were excited by a pulsed laser (PDL 800-B system with an external trigger), with a wavelength and frequency of 632 nm and 1 MHz, respectively. The photoluminescence photons were counted by a Picoharp 300 after being pre-amplified by a pre-amplifier module (PAM102, PicoQuant).

XPS and UPS. XPS measurements were carried out on an XPS AXIS Ultra DLD (Kratos Analytical). An Al K_α (1,486.6 eV) X-ray was used as the excitation source. UPS measurements were carried out to determine the work function of the materials, and a He discharge lamp, emitting ultraviolet energy at 21.2 eV, was used for excitation. All UPS measurements of the onset of photoemission to determine the workfunction were performed using standard procedures with a −9 V bias applied to the samples.

References

49. You, J. *et al.* Metal oxide nanoparticles as electron transport layer in high performance and stable inverted polymer solar cells. *Adv. Mater.* **24,** 5267–5272 (2012).